CHAPTER 6

Effect of horizontal and vertical averaging and layering on retrieval schemes of cloud properties

The following sections discuss the effect of averaging and layering on observations of nadir reflectances and on a measure proportional to cloud top height. In section 6.1 realistic LWC profiles are utilised to study the effect of vertical layering and averaging on nadir observations in an absorbing and non-absorbing environment. Note that vertical variability were neglected in the previous sections. Thereafter, 1d and 2d horizontal averaging effects on nadir radiances and measures proportional to cloud top height are studied. The investigation is separated in a study based on radiance observations made by *casi* and 3d RT simulations. Closed single layer clouds and complex cloud systems are considered. The outcome approves the necessity to apply the analysis presented in the previous sections to well-defined situations. Both, the vertical and horizontal averaging and layering effects, consider the difference between homogeneous and heterogeneous mixing. In the last section, the problem of enhanced photon path length (due to multiple scattering) in an absorbing medium is addressed. A parameterisation of the mean photon path with optical thickness and effective radius is presented.

6.1. Vertical layering effects on nadir reflectances

Usually the vertical distribution of cloud properties is neglected or determined on the basis of adiabaticity, if input fields for RT simulations are generated to derive cloud properties or to study 3d RT effects. In this section, the effect of vertical layering on simulated nadir reflectances is investigated. Four different types of LWC profiles form the basis of this study: one adiabatic profile and three non-adiabatic profiles simulated by an LES model. In order to determine optically relevant cloud properties from the LWC profiles, homogeneous and heterogeneous mixing are considered. Besides the difference between the adiabatic and the other cloud profiles, the effect of vertical averaging is investigated.

The three non-adiabatic LWC profiles are taken from the LES simulations presented in section 3.3. Due to the strong variability of the LWC profiles even on small scales, local averaging is not appropriate to define characteristic profiles. Instead, visual inspection of single profiles results in the cases used for the study in this section. The criteria for choosing a profile are: 1) different physical effects which result in distinct LWC profiles and 2) relatively smooth slopes at cloud base and top for further processing.

Figure 6.1 shows the chosen LWC profiles plus the adiabatic profile versus height above cloud base. The adiabatic LWC profile (*adiab*) is calculated with a condensation rate of c_w = 0.002 g m^{-4}, as it is found on average in the LES. All other LWC profiles differ significantly from the adiabatic profile. The naming is oriented at the underlying physical process which causes this deviation. The strong maximum of LWC near cloud top is caused by radiative cooling (*rad cool*): The cloud layer is heated from the surface and emits thermal radiation to overlaying cool atmospheric layers. If this happens, the decrease in temperature gives reason to further condensation. At low heights the profile is slightly overadiabatic. The reason can be a change of the condensation rate due to local variations of thermodynamic parameters. In other words, the local c_w is larger than 0.002 g m^{-4} and the profile may actually be adiabatic. Another possibility is, that the effect has dynamical reasons: Circulation around convective cells may advect profiles which are characterised by

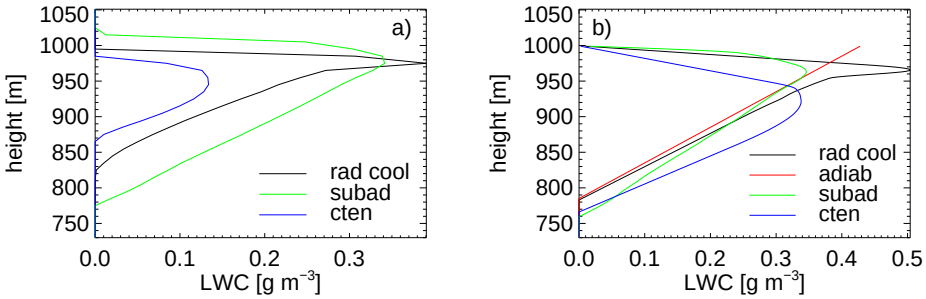

FIGURE 6.1. LWC profiles from LES simulations (left panel). The right panel shows the same profiles plus the adiabatic one for constant LWP (see text for details).

larger LWC. This is also observed in the cloud top entrainment profile (*cten*). In this case, dry and cold air is entrained from overlaying layers into the upper cloud layers. The last case is denoted as subadiabatic profile (*subad*). On the one hand, it can be the consequence of a locally smaller c_w (compared to 0.002 g m^{-4}). On the other hand, subadiabatic profiles are expected, if the release of latent heat is considered during the ascent of cloud parcels. Additionally, this profile is characterised by cloud top entrainment but to a lower degree as the *cten* profile.

In order to allow a comparison between the effects of the different profiles on nadir reflectances, LWP is adjusted to a constant value of ~46 g m^{-2}. The conditioning is carried out in two steps. First, the original profile is interpolated to height increments of 1 m using Akima interpolation (*Akima*, 1970). Secondly, the interpolated profile is scaled to a certain geometrical thickness so that the required LWP is reached. This is the reason to demand a certain degree of smoothness of LWC at cloud top and base. The outcome of this process is presented in Figure 6.1b. The preprocessing of LWC does not change the general shape of the LWC profiles. The cloud top height is kept fixed at 1 km, and the geometrical thickness is slightly larger than 200 m.

In case of the adiabatic profile, the input parameters for the *local estimate model* (see section 4.1) are calculated as outlined in section 3.4. The non-adiabatic profiles are subjected to homogeneous and heterogeneous mixing (see section 3.5). If heterogeneous mixing is investigated, the local cloud base is utilised for all three profiles: The *rad cool* and *cten* profiles, both from the stratus, were proved to be related to local thermodynamic processes. In case of the *subad* profile (taken from the cumulus) the local cloud base is lower than 1:15 h earlier, so that the local cloud base can be used (see section 3.5 for an explanation of both approaches).

The effect of vertical averaging is studied in terms of layer thicknesses Δz of 1, 5, 10, and 50 m and in terms of a vertical homogeneous case assuming a geometrical thickness of 200 m. σ_{ext} is simply averaged ($\omega_0 \approx 1$) while $\tilde{\beta}$ is determined according to Eq. 4.8, but here, cloud droplets are considered only. If the geometrical thickness differs from 200 m, the mean σ_{ext} is scaled with the ratio of the actual thickness to 200 m (homogeneous case). The same procedure is applied, if the number of layers is not an integer multiple of the actual thickness divided by the layer thickness.

With help of the *local estimate model* the nadir reflectance R is simulated for N=200 cm^{-3}, c_w=0.002 g m^{-4}, and a photon number of 10^7. The photon number ensures an accuracy of minimum 1%. 35 simulations are carried out: four different profiles, three of them with different mixing schemes, and five different layer thicknesses.

In Figure 6.2 the variation of the reflectance and optical thickness in dependence of the profile type and the mixing scheme is shown (Δz =1 m). The maximum reflectance difference of 6% is found between the heterogeneous *cten* and *subad* profile which must be

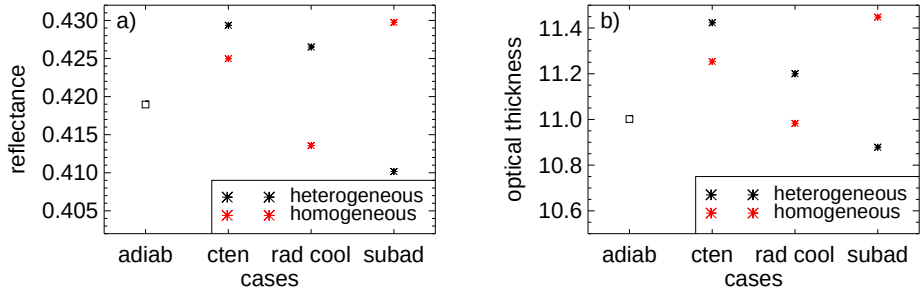

FIGURE 6.2. Reflectance (Fig. a) and optical thickness (Fig. b) versus profiles for two different mixing schemes (Δz =1 m). The abbreviations of the cases are given in the text.

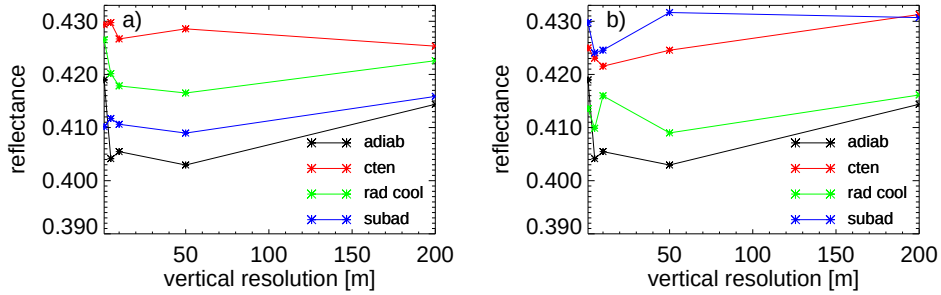

FIGURE 6.3. Behaviour of the reflectance dependent on profile type, mixing scheme, and layer thickness.

considered significant since the LWP is kept fixed in all cases. The reflectance correlates with the optical thickness, as can be seen by comparison of Figures 6.2a and b. The dependence of the optical thickness on the mixing scheme was outlined in section 3.5 and was found to be related to the degree of non-adiabaticity. If the average ratio of non-adiabatic LWC to the adiabatic values is determined, the *cten* and *rad cool* profiles are overadiabatic, and *subad* is indeed subadiabatic. Additionally, the difference from 1 is largest for the latter case which coincides with the largest difference between R of the homogeneous and heterogeneous case. These considerations explain the behaviour of the optical thickness in Figure 6.2b.

Figure 6.3 demonstrates the effect of vertical layering on the nadir reflectance. If the differences within each profile are studied, the maximum change of 4% is found for the *adiab* profile. The second highest is 2% (homogeneous mixing, *rad cool* profile). The optical thickness remains constant, if the layer thickness is changed (not shown). That means the observed effects can only be a consequence of variable phase functions (ω_0 is practically one). The phase function depends mainly on the radius, and largest variations of the radius are found for the *adiab* case. The dependence on Δz shows no systematic behaviour, and the effect is smaller in most cases, if compared to the dependence on the profile and mixing scheme (Fig. 6.2).

The analysis is extended to non-conservative media. It can be expected from the following considerations that the vertical variability of cloud properties may result in significantly larger effects, if absorption takes place: Figure 6.4 shows the photon path length distribution and the weighting function for the *adiab* and *cten* simulations. It can be expected from the continuous increase of LWC in the *adiab* profile, that σ_{ext}(*adiab*) is larger

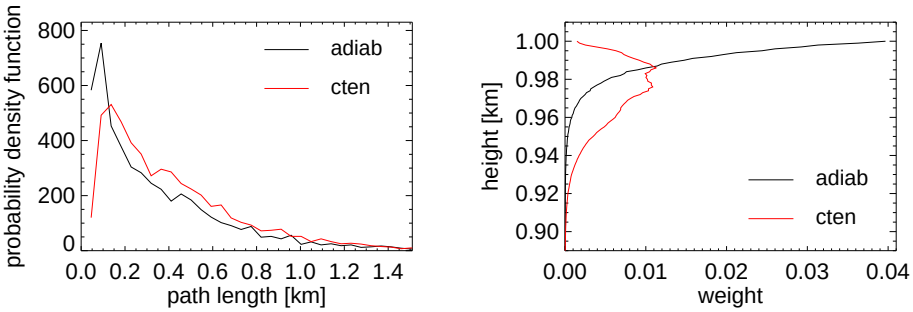

FIGURE 6.4. Photon path length distribution and weighting function versus height for the *adiab* and *cten* profile.

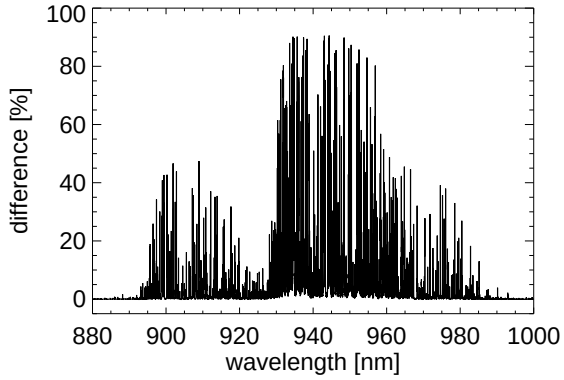

FIGURE 6.5. Difference between the normalised reflectance of the *adiab* and the *cten* profile. The spectral resolution is 0.01 nm.

at cloud top than σ_{ext}(*cten*). The large σ_{ext} at cloud top significantly reduces the probability for large photon path lengths what becomes evident when the maxima of the photon path length distributions are compared (Fig. 6.4a): The maximum of the *adiab* case is located at smaller path lengths than the maximum of the *cten* case (smaller LWC, smaller σ_{ext}). The same argumentation explains that the majority of the signal has its origin at cloud top in case of the *adiab* profile while the *cten* weighting function has a maximum ~20 m below cloud top (Fig. 6.4b). The effect of absorption may be more intense than the conservative effect because the extinction strongly depends on photon path length statistics, and therefore, the cloud top properties will govern the observed nadir reflectance. Looking at Figure 6.1, the largest variability of LWC is found at cloud top.

The determination of R in an absorption band is carried out for the $\rho\sigma\tau$-water vapour absorption band. The procedure is outlined in sections 4.2 and 5.3, but here, the calculations are not convoluted with a Gauss-function and have a spectral resolution of 0.01 nm. In Figure 6.5 an exemplary result is shown: The normalised reflectance is plotted against wavelength for the *adiab* and *cten* profile (Δz=1 m). The major result is that the reflectance of the *cten* profile is smaller than the reflectance for the *adiab* profile, independent of the wavelength.

The dependence on wavelength is transformed to a dependence on transmission by taking $\exp\left(-\sigma_a \text{ x } 1\,\mathrm{km}\right)$ and sorting the transmission in ascending order. Then, the difference of each normalised profile to the *adiab* profile is determined. The result is given in Figure 6.6, each panel for a different Δz. Also shown is the effect of the mixing scheme. The maximum difference of 90%, Figure 6.6a, is not given. The general issues are: 1) All

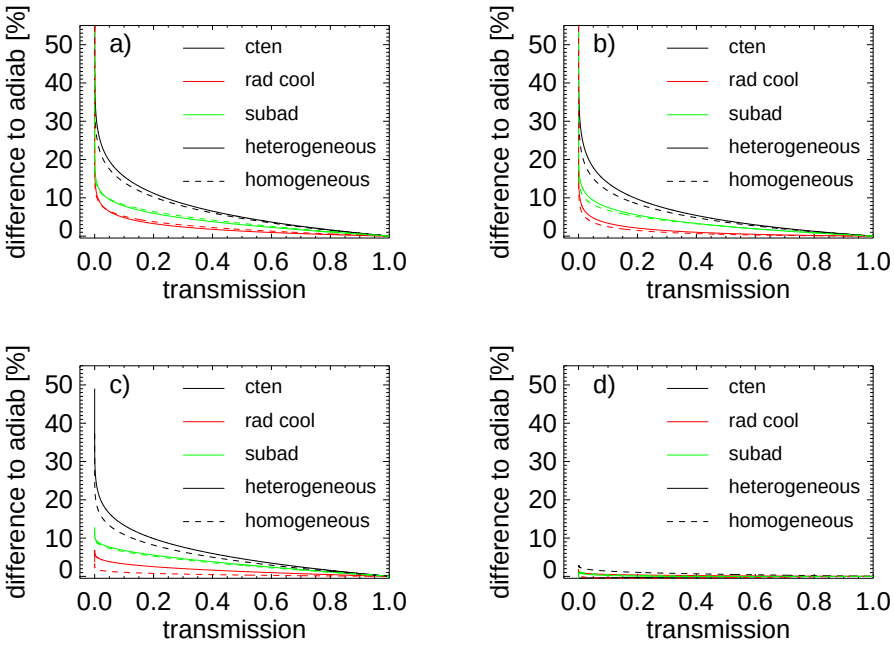

FIGURE 6.6. Difference between normalised reflectance of non-adiabatic and adiabatic profiles versus transmission. Each figure gives the result for a different layer thickness: a) Δz=1 m, b) Δz=10 m, c) Δz=50 m, and d) Δz=200 m. The dependence on the mixing scheme is also demonstrated.

differences are positive, 2) A strong increase of the effect with decreasing transmission, 3) The layer thickness is of minor importance, 4) The differences nearly vanish, if complete vertical homogeneity (Δz=200 m) is considered, and 5) The mixing scheme is almost negligible in this study. The positiveness of the difference has its reason in $\sigma_{ext}\,(z)$. σ_{ext} at cloud top is largest in the *adiab* case, followed by the *subad* and *rad cool* cases and is smallest in the *cten* case. The effect of σ_{ext} on the photon path length distribution was outlined before. A higher probability of larger photon path lengths, as observed for small σ_{ext} at cloud top, increases the intensity of absorption what explains the positiveness. The effect increases with increasing absorption since this effect is intensified. The major finding is that the extinction at cloud top is of major importance in this study. The effect of the layer thickness on the difference decreases with increasing Δz, especially for the *subad* and *rad cool* profiles, but not significantly for the *cten* profile (if $\Delta z \leq 50$ m). The *subad* and *rad cool* profiles are characterised by small spatial features, e.g. local maxima of LWC (see *rad cool* profile in Fig. 6.1b). In contrast, the dominating feature of the *cten* profile extends over scales larger than 50 m. In Figure 6.6d the remaining discrepancy can arise only from phase function differences.

The investigation of the effect of vertical averaging is estimated as the difference of each $R\,(\Delta z)$ to the vertical homogeneous case. The outcome is presented in Figure 6.7. The smallest and largest difference of around -35% and 90%, respectively, are not shown in Figure 6.7a. In general, the difference mainly depends on absorption intensity. The effect is the smallest for the *subad* case, followed by the *rad cool* case. The strongest effect can be observed for the *adiab* and *cten* profiles, and remarkable is the opposite sign between both cases. Again, the explanation can be found by a closer look at σ_{ext}. Figure 6.8 shows profiles of σ_{ext} of both cases. The dashed line indicates the value of σ_{ext} for vertical

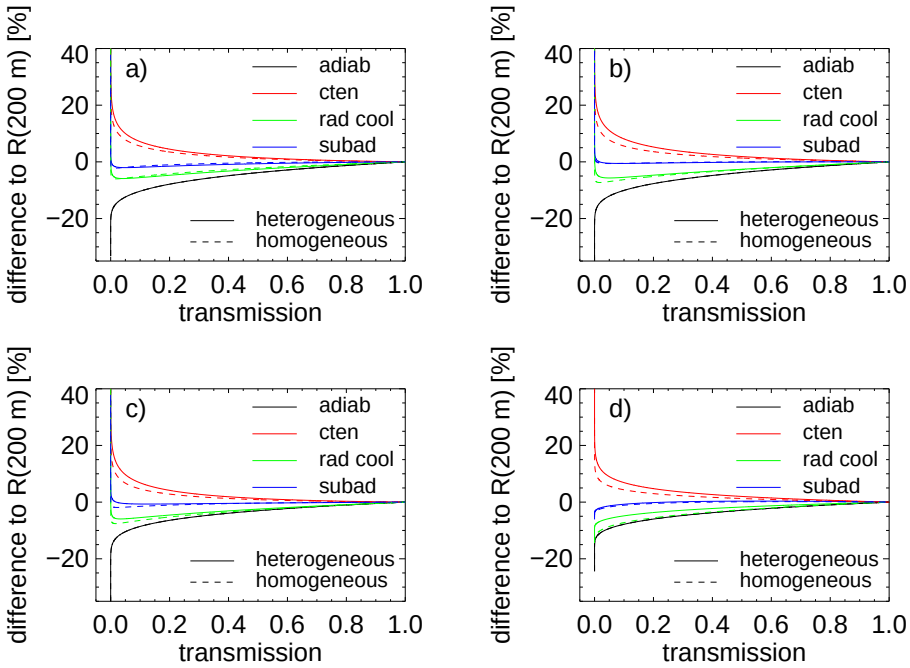

FIGURE 6.7. Difference between normalised reflectance and vertical homogeneous case versus transmission. Each figure gives the result for a different layer thickness: a) Δz=1 m, b) Δz=5 m, c) Δz=10 m, and d) Δz=50 m. The dependence on the mixing scheme is also demonstrated.

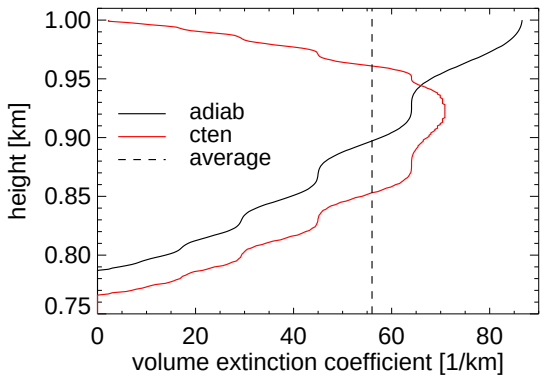

FIGURE 6.8. Profiles of the volume extinction coefficient, in black for the *adiab* and in red for the *cten* case. The dashed vertical line gives the value for vertical homogeneity.

homogeneity. The average σ_{ext} is smaller than σ_{ext} at cloud top for the *adiab* profile and larger for the *cten* profile.

The conclusions are that the nadir reflectance of conservative media does not depend significantly on the LWC profile. As soon as absorption takes place, the knowledge of the LWC profile should be given, especially at cloud top and if large absorption intensities are considered. The dependence on layer thickness and mixing scheme is of minor importance. The problems related to generally unknown LWC profiles can be reduced, if observations

in quasi-adiabatic areas are carried out (assumedly in the cores of convective cells where largest signals can be expected).

6.2. Horizontal averaging effects in measured and simulated remote sensing fields

In this section the effect of horizontal averaging on nadir reflectances and measures proportional to cloud top height is studied. The effects are investigated based on measurements performed with *casi* during the BBC campaign (sections 2.1.1 and 2.2) and on 3d RT simulations utilising the *local estimate model* and the LES cloud fields presented in section 4.1 and Figure 3.2, respectively. The first part of this section concentrates on the observations and the second on the simulations.

To study the effect of horizontal averaging on nadir reflectances, the reflectance at 755 nm is calculated from the observed radiance by Eq. 4.6, with F_0 from *Thullier et al.* (1998). Since a cloud top height retrieval from *casi* does not exist so far, a measure related to cloud top height is defined: R(761 nm) / R(755 nm). The ratio is proportional to the transmission T and can be approximated by $T = \exp(-\sigma_a l)$ with l being the photon path from the sun via the cloud to the sensor. The approximation is strongly simplified but demonstrates the relation between absorption intensity and cloud top height.

Even though *casi* provides 2d radiance observations, only the nadir reflectance is utilised for the upcoming investigations. The necessity for this follows from *casi*'s smile effect (section 2.1.1): The dependence of the spectral band setting on spatial pixels affects the measurement in the oxygen A-band at 761 nm. If the observations were taken over land, where a constant ratio can be expected, large variations of the ratio were found, if calculated for all spatial pixels.

The artificial degradation of the spatial resolution is done as follows:

$$\begin{aligned} \langle R \rangle_i &= \frac{1}{N-x} \sum_{i=0}^{i=N-x-1} R_{755}(x : x+i) \text{ and} \\ \langle r \rangle_i &= \frac{1}{N-x} \left(\sum_{i=0}^{i=N-x-1} R_{761}(x : x+i) \right) / \left(\sum_{i=0}^{i=N-x-1} R_{755}(x : x+i) \right) \end{aligned} \quad (6.1)$$

for the reflectance and the ratio, respectively (N: total number of data points, $0 \leq i \leq N-1$: data index, and x: start position).

Figure 6.9 shows the results after the artificial degradation of the resolution. The effect of horizontal averaging on nadir reflectances is shown in Figures 6.9a and c and on the ratio in Figures 6.9b and d. Each effect is plotted versus scale which is determined from i with the help of duration since leg start and ground speed measurements. $\langle R \rangle_i$ and $\langle r \rangle_i$ are normalised to their values at maximum scale. The red lines mark the uncertainty levels. In case of the reflectances the level is set to 3%, see section 2.1.1. The level for the ratio is calculated to 1.7%. The value stems from the error estimate of the cloud top pressure retrieval, which was found by *Preusker et al.* (2004) to be 20 hPa. Utilising the modified k-distribution of *Bennartz and Fischer* (1999), the transmission is determined as a function of pressure: If the pressure changes by 20 hPa around 850 hPa, the transmission varies by 1.7%.

Figures 6.9a and b refer to observations over closed single layer clouds: eight sections from 06, 13, 20, 22, and 23 September 2001. Figures 6.9c and d consider a variety of complex cloud situations: broken two layer clouds (06 and 23 September 2001), broken single layer clouds (22 September 2001), and a cloud layer with on average increasing reflectance along the flight track (06 September 2001). Figures 6.9a and c show effects of horizontal averaging on nadir reflectance of up to 70% and span a range of maximum 90%. In case of the closed single layer cloud decks and with one exception, the effect is significant for scales up to 4 km. All complex cloud cases stay above significance level at least up to a spatial scale of 12 km while the effect for the broken cloud case reaches scales of 25 km before dropping below the 3% level. The picture changes dramatically, if

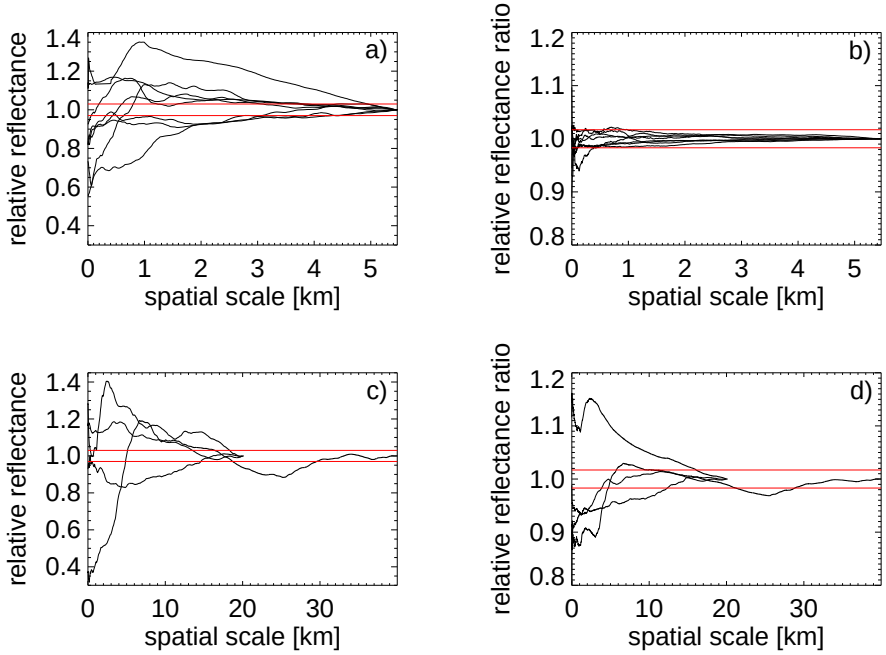

FIGURE 6.9. Effect of horizontal averaging on nadir reflectances and window to absorbing channel ratios, each normalised to its value at maximum scale. The different black lines belong to different data sets: Fig. a and b are based on data recorded over closed single layer clouds while Fig. c and d consider a variety of complex cloud situations (two layer clouds and broken cloud fields). The red lines mark the uncertainty level of the radiance measurement, 3%, and the minimum error for cloud top height retrieval, 1.7%.

the effect of horizontal averaging on the reflectance ratio is considered (Figs. 6.9b and d): The maximum effect is 15%, again for the broken cloud case, and in both cloud cases the range of the effect is strongly reduced. In case of the closed single layer clouds, the effect hardly reaches the sensitivity level for scales below 1 km and is not relevant at larger scales. The scale based results for the complex cloud cases remain valid but to a lower degree in intensity.

The results for the closed single layer clouds can be explained with relatively strong variations in reflectance due to variations in optical thickness and cloud top in combination with shadowing. Since the cloud top variations result in relatively small photon path length changes, if related to the direct path through the atmosphere, the effect vanishes, if the ratio is considered. In general, the complex cloud cases are characterised by photon path length changes within the observed scene, either due to a large variability of cloud top, e.g. in the two layer cloud case, or due to the brokenness of the cloud deck. Not shown is, that the relative reflectance and ratio at small scales strongly depend on the location of the start value of the averaging. It is intuitively obvious that starting with cloud shadows or with dark surfaces results in different findings than starting with bright clouds. However, the large scale mean is not significantly affected.

These considerations show the difficulty in finding representative means for reflectances and higher order products. From the BBC 2001 *casi* catalog, the log book, and the high resolution of *casi*, it can be ensured that the results presented in Figure 6.9b are indeed related to simple cloud situations. It is usually not possible to characterise the subpixel variability of satellite measurements which have orders of magnitude larger food

TABLE 6.1. Mean ($\langle R \rangle$) and standard deviation (σ_R) of reflectance fields simulated based on the adiabatic assumption and on heterogeneous and homogeneous mixing.

Cloud case	Parameter	Adiabatic	Heterogeneous	Homogeneous
Sc	$\langle R \rangle$	0.167	0.153	0.172
	σ_R	0.084	0.083	0.081
Cu	$\langle R \rangle$	0.099	0.078	0.099
	σ_R	0.087	0.079	0.086

prints (see Table 1). If the observations of satellites with different resolution are compared e.g. for validation purposes, the results of this section show that great care is necessary. Due to the strong dependence on the start value, a simple reduction of the resolution might not guarantee a successful validation. The exact allocation of both observations need to be given to avoid this problem.

These results are compared to the results retrieved from 3d RT simulations. In particular, the difference between 1d and 2d averaging is studied. The LES fields presented in Figure 3.2 are utilised. The microphysical parameters are determined as outlined in section 3.5. The averaging study is preceded by a short discussion of the effect of the mixing schemes on the reflectance fields. The reflectances of the stratus and the cumulus are computed for A=0 and 0.4 as well as θ_0=0° and with 10^5 photons per horizontal box. The uncertainty of these simulations is addressed by comparing two independent simulations with identical input, here the heterogeneous mixing for the cumulus cloud. The difference between both simulations amounts to 0.2% for $\langle R \rangle$ and 0.1% for σ_R. In Figure 6.10 the reflectance fields are shown: Upper and lower panels refer to the stratus and cumulus, and left and right panels to heterogeneous and homogeneous mixing, respectively. To make comparisons between both mixing schemes easier, the reflectance range for each cloud case is kept fixed. In fact, the heterogeneous cases have slightly smaller maxima than the other mixing cases. Besides the maxima, visual inspection reveals higher average reflectances for the homogeneous than for the heterogeneous plots for both cloud types. The mean and the standard deviation of the reflectance fields are summarised in Table 6.1. Additionally, the parameters for an adiabatic cloud field are provided. The cloud base and LWP of the cumulus and stratus are locally kept fixed and define the microphysical parameters taken from the adiabatic microphysical model (section 3.4, with N=200 cm^{-3} and c_w=0.002 g cm^{-4}, as in the previous section). In consequence, the cloud top height changes dependent on the deviation of LWC$'$ from adiabatic predictions. Another option would have been the preservation of cloud base and top height but the changes in (mean and local) optical thickness are dramatic in this case and make a comparison impossible. In general, the homogeneous case yields the largest, the adiabatic medium and the heterogeneous the smallest mean reflectances. σ_R is in general largest for the adiabatic case. σ_R is almost constant for all cases, if the stratus is considered but varies significantly for the cumulus. Similar conclusions can be drawn for $\langle R \rangle$. Due to the larger cloud fraction and mean optical thickness $\langle R \rangle$ is approximately twice as large in the stratus case, if compared to the cumulus.

If a scatterplot of τ_{hom} versus τ_{het} is considered (not shown), τ_{hom} is generally larger than τ_{het} with the exception of a small region at low τ_{hom}. The former together with $\langle R \rangle$ being larger for homogeneous than for heterogeneous mixing reveals that LWC profiles are on average subadiabatic (see section 3.5). The latter is due to extremely overadiabatic profiles and is found at the periphery of cumulus clouds. Probably dry air is entrained from the cloud side and base, leaving cloud top parts almost unchanged but increasing the apparent slope of LWC significantly. In both cases, σ_R is largest for the adiabatic assumption. This may be related to the variability of σ_{ext} at cloud top, being largest in the adiabatic case. However, this aspect is very complex, since horizontal photon transport

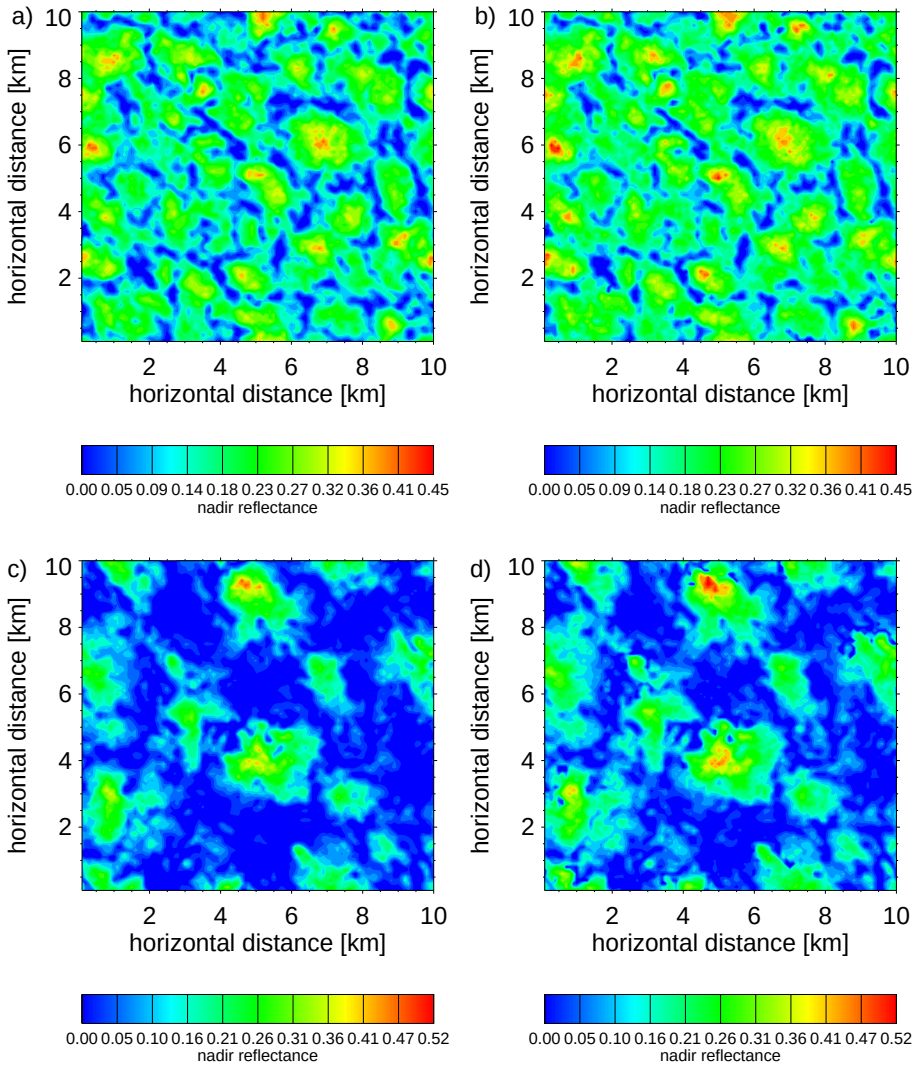

FIGURE 6.10. Reflectance fields simulated on the basis of the LWP fields presented in Figure 3.2. Figs. a and b show reflectance of the stratus and Figs. c and d of the cumulus. The left panels are related to heterogeneous and the right panels to homogeneous mixing. The maxima of the heterogeneous cases are slightly smaller than those of the homogeneous cases. To make the comparisons between both mixing schemes easier the range is kept fixed to the range of each homogeneous case.

between cloud tops and/or cloud parcels blurs the effect of cloud top extinction. It should be mentioned, that the different definitions of cloud base (heterogeneous mixing) result in large differences: $\langle R \rangle$ and σ_R are 0.066 and 0.070, respectively, if the 1%-percentile is chosen to define cloud base. Both values are smaller than those given in Table 6.1.

The horizontal averaging analysis is applied to the simulations with A=0.4 and θ_0=0°. Oxygen absorption is treated as outlined in section 4.2: Monochromatic calculations are carried out and then convoluted with a Gauss function (FWHM=2.8 nm, centred at 761 nm). The simulations are carried out without a background atmosphere, i.e. cloud scattering and absorption are considered but not contributions from air molecules and aerosols. In

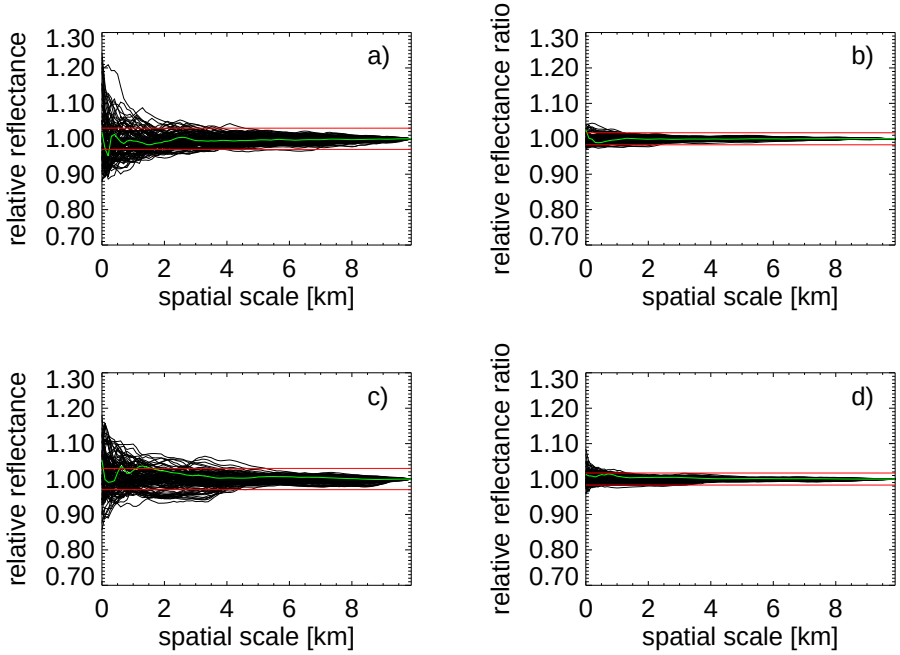

FIGURE 6.11. Effect of horizontal averaging on nadir reflectance (left panels) and window to absorption channel ratio (right panels), each normalised to the large scale value. The black lines are related to horizontal transects (100 in each panel), and the red lines give the uncertainty measures (similar to Figure 6.9). The green lines give the results, if averaged over the complete 2d field. Note, that in this case the effect depends on the square of the spatial scale in km^2. The upper (lower) panels show the results for simulations based on the stratus (cumulus), see Figure 3.2 to get an impression of the LWP fields.

consequence, the transmission above the model domain, with cloud top at 1 km, is multiplied to the reflectance to account for the additional absorption above the cloud layer. The artificial degradation is done as in Eq. 6.2. The averaging is carried out for both horizontal dimensions.

The outcome of the analysis is summarised in Figure 6.11. The effect of horizontal averaging is plotted in terms of reflectance (left panels) and ratio of window to absorption channel (right panels), each normalised to the large scale value, versus spatial scale. The black lines are related to horizontal transects while the green lines give the results for 2d averaging. In case of 2d averaging, the x-axis needs to be considered as the square of the spatial scale. The red lines mark the uncertainty level. The upper panels refer to the stratus and the lower to the cumulus.

The effect of 1d horizontal averaging on the reflectance is relevant for scales up to 4.5 km. The maximum variability of the effect is between +20% and -12% and drops rapidly below the uncertainty level. This decrease is slightly less intense in the cumulus case. If the ratio is considered, the effect hardly reaches the significance level and if so, only at scales smaller than 1 km. The effect based on 2d averaging is in all four plots below or close to the uncertainty measures. The maximum effect is 5% (reflectance cases) while the maximum scale, where the effect is above significance level, is 1.5 km (Fig. 6.11c). One aspect which is not shown here is, that the results for 1d averaging are almost independent on whether the averaging is carried out along the x- or y-axis. The effect of 2d averaging is not significantly affected, if the starting position is changed (in contrast to 1d averaging).

The effect of horizontal averaging is more intense, if the reflectance and not the ratio is considered (as the results from observations). Furthermore, the effect on the ratio is not significant, if relatively homogeneous cloud systems are investigated. In general, the studies based on observations of relatively homogeneous clouds could be verified. The complex cases could not be investigated, as no reliable cloud data is available. The stratus and the cumulus have a cloud coverage of 97% and 83% and mean optical thicknesses of 4.0 (maximum 13) and 2.2 (maximum 19), respectively, and in both cases, the cloud top variability is very small with values around 1 km. Therefore, similar results as for the observed complex clouds are not found here, since the clouds do not exhibit appropriate variability. The 2d averaging has significantly lower effects than 1d averaging and hardly reaches the significance level, even if the reflectance is studied. The reason is that the amount of pixels for 2d averaging equals the square of pixels for 1d averaging.

These investigations demonstrate that great care is required, if observations of different spatial resolution are compared. Not only the artificial adjustment of the resolution but also the exact allocation is required. If 2d, and not 1d, observations are considered, the averaging is less problematic, since the mean is calculated for much more data points. However, the impact may remain significant, if complex cloud systems are studied. Therefore, the simulations should be extended to broken and multi-layer clouds. Synchronised *casi* and satellite observations should be utilised to examine the practicability of allocation and averaging in order to compare the measurements.

6.3. Parameterisation of mean photon path length

Several remote sensing retrievals of cloud properties rely on observations in absorption channels, e.g. the cloud top pressure retrieval on the oxygen A-band channels (*Preusker et al.*, 2004). Many retrieval schemes suffer from poor representations of clouds in input fields for RT simulations which form the basis of the inversion. For example, if clouds are parameterised with a single albedo value only, the absorption intensity is significantly underestimated because contributions from lower layers are neglected but certainly have significant effects, especially in the presence of multiple scattering. In this section, an outline is presented to account for an increase of gas absorption due to an increase of photon path length in the presence of clouds. The parameterisation is based on cloud properties, i.e optical thickness and effective radius, which can be retrieved with standard inversion algorithms and are diagnostic parameters in global circulation models.

In the previous section various realistic cloud profiles were investigated to see their effect on nadir reflectances in the presence of absorption. The major conclusion was that the absorption intensity strongly depends on the extinction at cloud top and therefore on the actual cloud profile. Since information on cloud profiles is usually not available in remote sensing of cloud properties by passive observations in the visible and near infrared, adiabatic cloud profiles form the basis of this study.

In order calculate microphysical cloud properties, the β^2-scheme, presented in section 3.4, is utilised. Four droplet number concentrations, N=50, 100, 200, and 400 cm^{-3}, covering air masses from clean to polluted, and optical thicknesses ranging from 1 to 170 are chosen together with c_w =0.0019 g m^{-4} to drive the droplet growth model. The predefinition of the optical thickness results in a variable cloud thickness. The vertical profiles of cloud properties are fed to the *classical Monte Carlo model* which provides the photon path length distribution, $P(l)$. The mean photon path length, $\langle l \rangle$, is then determined by:

$$\langle l \rangle = \int_0^\infty l P(l)\, \mathrm{d}l. \tag{6.2}$$

First, the relation of $\langle l \rangle$ to the geometrical thickness H is considered. Figure 6.12 shows $\langle l \rangle$ versus H. The asterisk mark the various sampling points of the simulations. The linear relation between both values is obvious and is expected from diffusion theory (*Davis et al.*, 1997a): The photons probability to leave the cloud, either through cloud base or top,

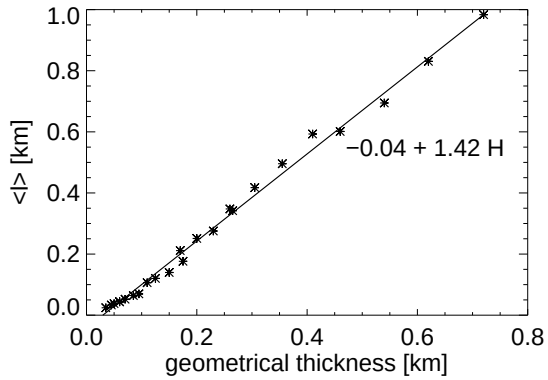

FIGURE 6.12. Mean optical path length versus geometrical cloud thickness. Each sampling point (asterisk) presents a simulation of specific N and τ. A linear relationship, $\langle l \rangle$=-0.04 + 1.42 H, can be seen with slight variations for different microphysics.

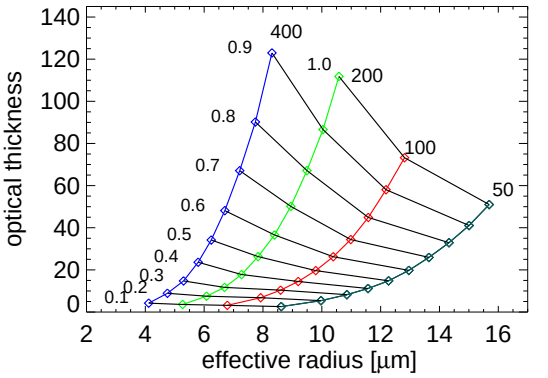

FIGURE 6.13. Isolines of mean path length ranging from 0.1 to 1 km (black lines). The phase space is defined by the effective radius and the optical thickness. Also shown are lines of constant cloud droplet number concentration in units of cm^{-3} (coloured lines).The simulations were performed with the sun at zenith and a nadir viewing observer.

is low for a large H. The dominant role of H is altered slightly by varying microphysics, in particular from different degrees of asymmetry of the phase function. Unfortunately, the retrieval of H from observations in the visible and near infrared is not unique because the cloud thickness and its cloud top height have opposite effects on the radiance measurements and cannot be separated.

Therefore, the dependence of $\langle l \rangle$ on τ and r_{eff} is considered in the following. r_{eff} is calculated as proposed by *Brenguier et al.* (2000):

$$r_{eff} = \frac{5}{6} \left(\frac{c_w}{4/3\pi\rho_w} H \right)^{1/3} N^{-1/3} \tag{6.3}$$

with ρ_w being the density of water. The results are given in Figure 6.13 (A=0 and θ_0=0°). On the x-axis the effective radius and on the y-axis the optical thickness are plotted. The coloured lines present isolines of N and the black lines isolines of mean photon path length.

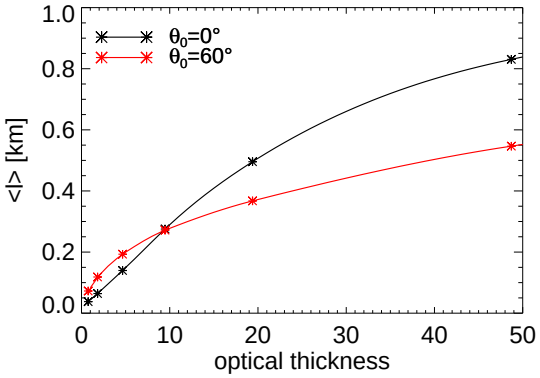

FIGURE 6.14. Mean path length versus optical thickness for θ_0=0° and 60° (A=0, N =100 cm^{-3}).

TABLE 6.2. Mean photon path lengths in km for the simulations discussed in section 6.1 (Δz=1 m).

	adiab	*cten*	*rad cool*	*subad*
heterogeneous	0.365	0.426	0.370	0.405
homogeneous	0.365	0.422	0.380	0.416

$\langle l \rangle$ ranges from 0.1 to 1 km. The isoline of $\langle l \rangle$=1 km is been extended to N =400 cm^{-3} because $\langle l \rangle$ asymptotically approaches $\langle l \rangle$=1 km with increasing optical thickness. In general $\langle l \rangle$ increases with increasing τ and r_{eff}. Noticeable is the increasing slope of the isolines of $\langle l \rangle$ with increasing optical thickness: At low optical thicknesses $\langle l \rangle$ is almost constant over a wide range of r_{eff}, but if τ increases more and more isolines of $\langle l \rangle$ are intercepted. In contrast, a wide range of r_{eff} may result in almost all presented $\langle l \rangle$ with the exception of small effective radii only.

The above outcome certainly depends on sun zenith angle and/or viewing direction. An exemplary analysis is carried out for θ_0=60° and N=100 cm^{-3} and shown in Figure 6.14. If the optical thicknesses is small, i.e. τ<10, the larger sun zenith angle results in larger mean photon path lengths, if compared to the θ_0=0° case. This observation is reversed for τ>10. The effect at low optical thicknesses can be explained by an increased direct photon path at high sun zenith angles. The less stronger increase of $\langle l \rangle$ at τ>10 is due to an increased probability of photons to remain in layers near cloud top and to leave the cloud in an upward direction. It is emphasised here, that these results were received for a surface albedo of A=0. An exemplary investigation with A=0.4 revealed a significant increase of the mean photon path for low optical thicknesses due to multiple scattering between cloud and surface. The increase almost vanishes for large optical thicknesses, since less and less photons are able to reach the ground, get reflected, pass the cloud a second time, and finally reach the detector.

Based on the simulations presented in the previous section a short discussion of the effect of realistic profiles on $\langle l \rangle$ is given. In Table 6.2, $\langle l \rangle$ is provided for the profiles presented in section 6.1. All realistic profiles are characterised by a larger $\langle l \rangle$ than the *adiab* profiles due to the presence of lower extinction at cloud top. The maximum difference is around 14% and is found for the *cten* profile which is characterised with lowest σ_{ext} over large cloud top regions.

Given τ and r_{eff}, e.g. through a retrieval scheme after *Nakajima and King* (1990), a mean photon path length can be determined. The additional radiative effect of the photon path in the cloud on a measurement in the presence of gas absorption can then be estimated

by $1 - \exp\left(-\sigma_a\left(\lambda\right)\left\langle l\right\rangle\right)$ with $\sigma_a\left(\lambda\right)$ the average vertical gas absorption below cloud top. Furthermore, $\langle l\rangle$ can be used as additional input parameter in the development of a retrieval scheme to avoid time consuming RT simulations. Finally, τ and r_{eff} are diagnostic variables in global circulation models. The parameterisation may offer a way to increase the accuracy of GCMs, if in addition to the optical thickness the effective radius is used to determine photon path length statistics.